

## Journal Pre-proof

Fully-coupled hydroelastic modelling of a deformable wall in waves

Zhengyu Hu, Luofeng Huang, Yuzhu Li

PII: S0378-3839(22)00158-2

DOI: <https://doi.org/10.1016/j.coastaleng.2022.104245>

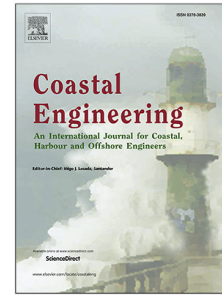
Reference: CENG 104245

To appear in: *Coastal Engineering*

Received date: 1 June 2022

Revised date: 2 October 2022

Accepted date: 28 October 2022



Please cite this article as: Z. Hu, L. Huang and Y. Li, Fully-coupled hydroelastic modelling of a deformable wall in waves. *Coastal Engineering* (2022), doi: <https://doi.org/10.1016/j.coastaleng.2022.104245>.

This is a PDF file of an article that has undergone enhancements after acceptance, such as the addition of a cover page and metadata, and formatting for readability, but it is not yet the definitive version of record. This version will undergo additional copyediting, typesetting and review before it is published in its final form, but we are providing this version to give early visibility of the article. Please note that, during the production process, errors may be discovered which could affect the content, and all legal disclaimers that apply to the journal pertain.

© 2022 Published by Elsevier B.V.

# Fully-coupled hydroelastic modelling of a deformable wall in waves

Zhengyu Hu<sup>a</sup>, Luofeng Huang<sup>b</sup>, Yuzhu Li<sup>a,\*</sup>

<sup>a</sup>*National University of Singapore, Department of Civil and Environmental Engineering, Singapore*

<sup>b</sup>*Cranfield University, School of Water, Energy and Environment, Cranfield, UK*

---

## Abstract

The hydroelastic behavior of a vertical wall in periodic waves is investigated using a fully-coupled computational fluid dynamics (CFD) and computational solid mechanics (CSM) model. The present numerical model is verified against previous numerical and experimental results on wave evolution and structural displacement. Then the hydrodynamic characteristics and the structural responses of an elastic wall in periodic waves are parametrically investigated. It is demonstrated that wave reflection, run-up, and loading decrease as the wall becomes more flexible. The decreases also occur when the waves become shorter. With nonlinear wave propagation, both the displacement and the stress of the wall are larger in the shoreward direction than those in the seaward direction. The wall displacement has the same frequency as the exciting waves and the stress increases with the decrease of the ratio of the wave frequency to the wall's natural frequency. Considering the effect of flexibility, empirical formulae are proposed for predicting the wave run-up, loading, and maximum displacement of the wall. Besides, the optimization of the flexible wall is conducted by taking into account both the defense performance (i.e., transmission coefficient) and the structural integrity (i.e., maximum von Mises stress). Finally, the effect of the material damping is studied, which shows that the material damping has a negligible effect on the interaction between periodic waves and the elastic structure.

*Keywords:* Hydroelasticity, Deformable structures, Wave-structure interaction, Fully-coupled simulation, OpenFOAM

---

\*Corresponding author

Email address: [pearl.li@nus.edu.sg](mailto:pearl.li@nus.edu.sg) (Yuzhu Li)

---

## 1. Introduction

Sea-level rise, extreme marine events, together with increasing flood risk due to climate change put coastal communities at growing threats (Field and Barros, 2014; Ranasinghe, 2016; Toimil et al., 2020; Nicholls and Cazenave, 2010). The existing coastal and offshore structures are often designed as rigid in the majority of engineering practices. However, traditional hard structures have to suffer costly maintenance and repair, especially after extreme storm events. In many situations, they are old and poor-maintained, which increases the coastal vulnerability (Jin et al., 2015). Therefore, investigating and optimizing the characteristics of flexible structures subjected to waves can be a significant research direction.

Many studies were devoted to the interaction between waves and perfectly rigid structures (Huang et al., 2022). Reeve et al. (2008) numerically investigated the discharges of overflow and wave overtopping over a rigid seawall with various freeboard and slope conditions subjected to irregular waves. They derived empirical formulae to predict the discharges with consideration of the overflow and the wave overtopping effects. Hsiao and Lin (2010) studied solitary waves impinging on a rigid trapezoidal seawall with experimental and numerical approaches. They found that the maximum wave force often occurs with the minimum freeboard and the wave run-up to the overtopping stage, which might lead to substantial structural damage and instability. Ning et al. (2017) carried out a numerical study on the interaction between the focused wave and a vertical rigid wall through a higher-order boundary element method. They observed that wave nonlinearity can increase the wave pressure on the wall. Attili et al. (2021) numerically investigated the hydrodynamic characteristics of the landslide-tsunamis impacting dams considering the three-dimensional effects of both oblique waves and arch dams. They proposed empirical formulae for predicting the wave loading, run-up, overtopping volume, and maximum overtopping depth for dams.

However, it has been observed that steep-fronted rigid structures can induce full wave reflection, which can yield aggravated scour and impair the stability of the structure. Although it is yet to be built in practice, flexible structures showed better hydrodynamic performance and wave damping effect compared to rigid structures in the recent laboratory studies. For example, Sree et al. (2021) performed an experimental study on the evolution

36 of periodic waves interacting with a submerged viscoelastic plate. They re-  
37 ported that the most flexible plate placed close to the mean water level can  
38 yield a nearly complete cutoff of wave energy transmission. Nevertheless,  
39 to date, detailed laboratory studies on the interaction between progressive  
40 waves and steep-fronted flexible structures are lacking. A few analytical and  
41 numerical investigations have been conducted on the hydroelastic interaction  
42 between water waves and vertical walls. For example, He and Kashiwagi  
43 (2009) simulated the vibration of a vertical rigid wall connected to a linear  
44 spring at back under the impact of a nonlinear pulse-type wave. They found  
45 that the nonlinear effect can cause an obvious discrepancy in the wall's mo-  
46 tion compared with the linear analytical solution. Peter and Meylan (2010)  
47 analytically described the vibration of an elastic wall in linear waves based  
48 on a generalized eigenfunction expansion method. He and Kashiwagi (2012)  
49 later investigated the hydroelastic behavior of both the top-fixed and the  
50 top-free walls with a bottom-fixed end in a solitary wave based on the po-  
51 tential flow and the linear beam assumptions. They coupled the fluid and  
52 the solid by combining the boundary element method and the finite element  
53 model in a monolithic way (i.e., solving fluid and solid motions with a single  
54 solver). Akrish et al. (2018) simulated the elastic wall in an incident wave  
55 group by a high-order spectral method, where the linear beam model was  
56 applied. They found that the hydroelastic effect can relax or amplify both  
57 hydrodynamic characteristics (i.e., wave run-up and force) and structural  
58 oscillations. However, the linear assumptions used in the above numerical  
59 solutions for either the fluid or the solid may have limited accuracies when  
60 predicting the finite-strain structure and nonlinear wave interactions.

61 As such numerical simulations involve the interaction between two physi-  
62 cal domains, i.e., the fluid and the solid, some coupling algorithms have been  
63 developed for the numerical models. Dermentzoglou et al. (2021) adopted a  
64 one-way coupling of computational fluid dynamics (CFD) and finite element  
65 method (FEM) to investigate the failure of a recurved wall with different  
66 concrete classes. Sriram and Ma (2012) simulated the interaction between  
67 the breaking wave and an elastic wall with a simply support. The fluid and  
68 the solid were solved in a partitioned approach with a near-strongly coupling  
69 at the interface, i.e., fluid particles maintained their positions from the end  
70 of the previous time step during fluid-structure-interaction (FSI) iterations.  
71 Liao and Hu (2013) proposed a FDM-FEM model (where FDM stands for  
72 the finite difference method) to investigate the interaction between the sur-  
73 face flow and a thin elastic wall with large deformation. The standard linear

74 beam element was employed and coupled with the fluid using a conservative  
75 momentum-exchange method based on the immersed boundary method. Ku-  
76 mar and Sriram (2020) simulated the breaking wave impacting on an elastic  
77 wall with a linear beam theory. They strongly coupled the fluid and the  
78 solid based on an iterative scheme. To avoid the ideal linear assumptions  
79 that have been used in most of the previous studies, Tuković et al. (2018)  
80 and Cardiff et al. (2018) developed an open-source toolbox integrating the  
81 fluid and the solid fields using the finite volume method in the OpenFOAM  
82 framework. This integrated model can be used for both fluids with nonlinear  
83 dynamics and structures with nonlinear mechanical laws (i.e., the stress ten-  
84 sor is a nonlinear function of the displacement vector). Huang et al. (2019)  
85 combined this model with the wave generation toolbox waves2Foam (Jacob-  
86 sen et al., 2012) to investigate the hydroelastic effects of a nonlinear ice sheet  
87 in monochromatic waves. Huang and Li (2022) further improved the model  
88 to study the hydroelasticity of a submerged horizontal-plate breakwater in  
89 nonlinear waves. They observed a better wave-damping performance with a  
90 deformable plate. To the authors' knowledge, a detailed investigation of the  
91 nonlinear interaction between progressive waves and a vertical elastic wall  
92 has not been conducted yet.

93 The present work combines the IHFOAM wave-modeling toolbox (Higuera  
94 et al., 2013) with a fully-coupled FSI approach (Tuković et al., 2018; Cardiff  
95 et al., 2018) to study the hydroelasticity of a vertical wall in periodic waves,  
96 aiming to get an overall insight into the nonlinear wave evolution and the  
97 corresponding structural response. The paper is organized as follows. The  
98 computational approach is described in section 2 followed by the numerical  
99 setup in section 3. Thereafter, the FSI model is verified against the numerical  
100 results of He and Kashiwagi (2012) and validated against the experimental  
101 results of Didier et al. (2014), as in section 4. In section 5, simulations are  
102 conducted for an elastic cantilever wall with different bending stiffness un-  
103 der nonlinear wave loading. The hydrodynamic and structural behaviors are  
104 investigated and optimized. Empirical formulae are proposed for the wave  
105 run-up, loading, and wall displacement estimations. Besides, the effect of the  
106 material damping on the hydroelasticity is investigated. Section 6 provides  
107 the conclusions.

108 **2. Numerical method**

109 The present numerical model consists of computational fluid dynamics  
 110 (CFD) and computational solid mechanics (CSM) together with a fully-  
 111 coupled algorithm. The governing equations are listed as follows.

112 *2.1. Computational fluid dynamics*

113 The CFD model solves the Navier–Stokes equations for incompressible,  
 114 isothermal, and Newtonian flows:

$$\nabla \cdot \mathbf{u} = 0 \quad (1)$$

115

$$\frac{\partial(\rho\mathbf{u})}{\partial t} + \nabla \cdot (\rho\mathbf{u}\mathbf{u}^T) = -\nabla p + \nabla \cdot \boldsymbol{\tau} + \rho\mathbf{g} \quad (2)$$

116 where  $\mathbf{u}$  is the velocity vector of the water-air mixture,  $\rho$  is the density,  $p$   
 117 is the pressure,  $\mathbf{g}$  is the gravitational acceleration, and  $\boldsymbol{\tau}$  is viscous stress  
 118 tensor defined by  $\boldsymbol{\tau} = \mu (\nabla\mathbf{u} + \nabla\mathbf{u}^T)$ , in which  $\mu$  is the dynamic viscosity of  
 119 the fluid.

120 The laminar flow model is employed in this simulation following Huang  
 121 and Li (2022) since the turbulent effects are expected to be negligible in  
 122 the present cases (i.e., no wave breaking), which can effectively reduce the  
 123 computational costs. Free surface simulations utilize the IHFOAM model  
 124 (Higuera et al., 2013) for wave generation and absorption. The Volume of  
 125 Fluid (VOF) approach (Hirt and Nichols, 1981) is applied to capture the  
 126 water-air interface with a defined phase indicator ( $\alpha$ ) denoting the proportion  
 127 of the water volume in each discrete cell.  $\alpha$  varies from 0 to 1 with  $\alpha = 1$   
 128 denoting a cell full of water and  $\alpha = 0$  indicating a cell full of air. Its  
 129 transport equation is:

$$\frac{\partial\alpha}{\partial t} + \nabla \cdot (\mathbf{u}\alpha) + \nabla \cdot [\mathbf{u}_c\alpha(1 - \alpha)] = 0 \quad (3)$$

130 where  $\mathbf{u}_c$  is the interface compression velocity between air and water for the  
 131 purpose of reducing the numerical diffusion (Weller et al., 1998). Further-  
 132 more, the mixed density and viscosity can be weighted in terms of  $\alpha$ :

$$\rho = \alpha\rho_w + (1 - \alpha)\rho_a \quad (4)$$

133

$$\mu = \alpha\mu_w + (1 - \alpha)\mu_a \quad (5)$$

134 where  $\rho_w = 1000 \text{ kg/m}^3$  is the water density,  $\rho_a = 1 \text{ kg/m}^3$  is the air density,  
 135  $\mu_w = 1 \times 10^{-3} \text{ N} \cdot \text{s/m}^2$  is the dynamic viscosity of the water, and  $\mu_a =$   
 136  $1.48 \times 10^{-5} \text{ N} \cdot \text{s/m}^2$  is the dynamic viscosity of the air.

## 137 2.2. Computational solid mechanics

138 Considering finite strains of the solid domain, the nonlinear mechani-  
 139 cal constitutive law, i.e., Neo-Hookean hyperelastic law, as implemented in  
 140 Cardiff et al. (2018), is used to calculate the Cauchy stress. The integration  
 141 of the momentum equation in the total Lagrangian form (refer to the initial  
 142 undeformed configuration) is given as:

$$\int \rho_s \frac{\partial^2 \mathbf{D}}{\partial t^2} dV = \oint (J \mathbf{W}^{-T} \cdot \mathbf{n}) \cdot \boldsymbol{\sigma} dS + \int \rho_s \mathbf{g} dV \quad (6)$$

143 where  $\rho_s$  is the solid density,  $\mathbf{D}$  is the displacement vector,  $\mathbf{W}$  is the de-  
 144 formation gradient tensor given by  $\mathbf{W} = \mathbf{I} + (\nabla \mathbf{D})^T$ ,  $\mathbf{I}$  is the second-order  
 145 identity tensor,  $J$  is Jacobian matrix of  $\mathbf{W}$ , i.e.,  $\det[\mathbf{W}]$ , in which  $\det[\cdot]$  is  
 146 the determinant operator, and  $\mathbf{n}$  is the outward facing normal vector. The  
 147 Cauchy stress tensor  $\boldsymbol{\sigma}$  is a nonlinear function of the displacement vector:

$$\boldsymbol{\sigma} = G \text{dev}[J^{-2/3} \mathbf{W} \cdot \mathbf{W}^T] + \frac{\kappa}{2} \left( \frac{J^2 - 1}{J} \right) \mathbf{I} \quad (7)$$

148 where  $G$  and  $\kappa$  are the shear modulus and bulk modulus, respectively. They  
 149 can be calculated by Young's modulus  $E$  and Poisson's ratio  $\nu$ :

$$G = \frac{E}{2(1 + \nu)} \quad (8)$$

150

$$\kappa = \frac{E}{3(1 - 2\nu)} \quad (9)$$

## 151 2.3. Fully-coupled algorithm

152 A partitioned scheme is implemented for the interaction between the fluid  
 153 and the solid domains. This means that the fluid and solid domains can be  
 154 solved alternately, whilst the momentum and kinematic continuity at the  
 155 fluid-solid interface is satisfied by a two-way coupling algorithm based on the  
 156 Dirichlet-Neumann approach (Tuković et al., 2018). For all time steps, the  
 157 pressure and velocity fields can first be obtained for the fluid domain. Then

158 the fluid force is passed onto the solid interface where dynamic condition,  
 159 i.e., force balance, is satisfied:

$$\mathbf{n} \cdot \boldsymbol{\sigma}_{\text{fluid}} = \mathbf{n} \cdot \boldsymbol{\sigma}_{\text{solid}} \quad (10)$$

160 where  $\boldsymbol{\sigma}_{\text{fluid}} = \boldsymbol{\tau} - p\mathbf{I}$  is the stress in the fluid domain. Thereby the solid  
 161 domain can be solved with this Neumann condition (traction) at the interface  
 162 boundary. Then, the velocity of the solid interface is passed back to the  
 163 fluid interface using the Aitken under-relaxation approach, i.e., the relaxation  
 164 factor varies in the FSI iterations to reduce the displacement residual faster.  
 165 The fluid domain is therefore calculated with a Dirichlet condition of velocity  
 166 at the interface boundary, satisfying the kinematic condition:

$$\mathbf{u}_{\text{fluid}} = \mathbf{u}_{\text{solid}} \quad (11)$$

167 Meanwhile, the mesh of the fluid domain is updated for the next iteration. A  
 168 number of iterations are required for each time step to achieve a continuous  
 169 displacement across the interface:

$$\mathbf{D}_{\text{fluid}} = \mathbf{D}_{\text{solid}} \quad (12)$$

170 A flowchart of the present fully-coupled FSI algorithm is illustrated in Fig. 1.  
 171 In the present study, the tolerance of the displacement residual (i.e., the rela-  
 172 tive displacement between the fluid side and solid side interfaces) is specified  
 173 as  $1 \times 10^{-6}$  m which is a negligible value compared with the magnitude of  
 174 the displacement. Besides, the maximum number of FSI iterations per time  
 175 step is set as 60, which allows the convergence to be achieved in each time  
 176 step.



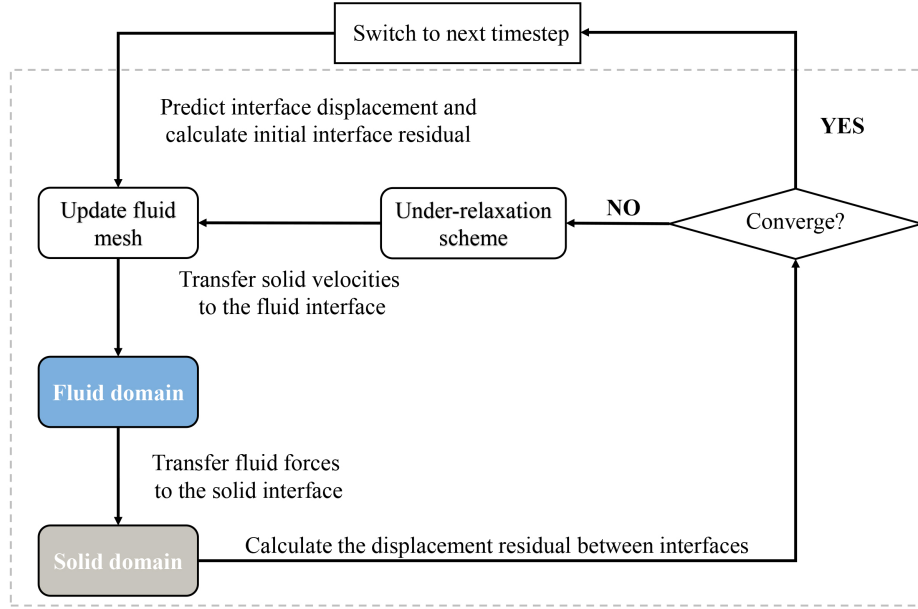


Fig. 1. Flowchart of FSI coupling algorithm.

### 177 3. Model setup and boundary conditions

178 A two-dimensional numerical flume is established as shown in Fig. 2.  
 179 The length and height of the flume are  $10L$  and  $2h$ , respectively, in which  
 180  $L$  denotes the wavelength and  $h$  is the water depth. The numerical flume is  
 181 built in a Cartesian coordinate system with  $x$ -axis pointing toward the wave  
 182 propagation direction and  $z$ -axis toward the vertical direction. The origin  
 183 of the coordinate system ( $O$ ) is set at the center of the flume's bottom. A  
 184 vertical wall is built in the center of the flume with a thickness of  $h/15$  and  
 185 a length ( $l$ ) of  $7h/6$ , resulting in a freeboard height of  $h/6$ .

186 Three wave gauges represented by WG1-WG3 are placed upstream of the  
 187 vertical wall. WG1 is at  $x = -10h$  and the interval distances of WG1-WG2  
 188 and WG2-WG3 are  $0.2L$  and  $0.3L$ , respectively. The reflected wave induced  
 189 by the vertical wall is estimated by a wave reflection analysis method of  
 190 Goda and Suzuki (1977) using the wave elevation records from wave gauges  
 191 WG1-WG3. Moreover, a wave gauge WG4 is placed on the front side of  
 192 the deformed wall. It moves along with the structural interface to observe

193 the run-up which is defined as the distance between the still water level and  
 194 the maximum water level on the wall. To accurately evaluate the transmis-  
 195 sion coefficient (i.e., shoreward energy propagation), WG5-WG7 are placed  
 196 downstream of the wall to perform the reflection analysis. Therefore, the  
 197 evaluation of the transmission coefficient is not influenced by the wave reflec-  
 198 tion from the outlet boundary (5% on average). Besides, the horizontal wave  
 199 loading per unit width of the wall  $F_x$  is obtained by integrating the pressure  
 200 on the solid interface.

201 For the applicability of analysis, the mechanical properties of the wall  
 202 are normalized into two non-dimensional parameters by the water depth. In  
 203 particular, the mass coefficient of the vertical wall is defined as:

$$\gamma = \frac{\rho_s b}{\rho_w h} \quad (13)$$

204 where  $b$  is the thickness of the wall. The stiffness coefficient of the vertical  
 205 wall is given by:

$$\beta = \frac{EI}{\rho_w g h^4} \quad (14)$$

206 where  $I = b^3/12$  is the moment of inertia of the wall.

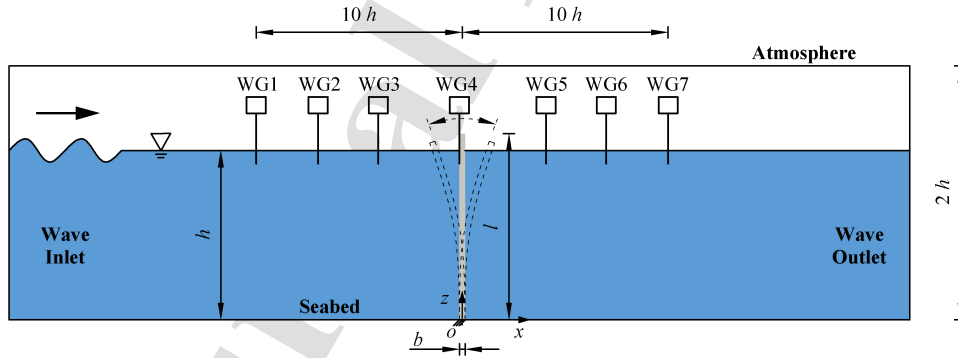


**Fig. 2.** Schematic diagram of the numerical flume (not to scale).

207 The present study is conducted on the model scale. The simulated struc-  
 208 tural and wave properties are listed in Table 1 with 60 cases in total. A  
 209 series of wall models (i.e., Models 1-9) with different mechanical properties  
 210 are considered for the present parametric investigation. The material stiff-  
 211 ness gradually increases from Model 1 to Model 9, and Model 10 (almost

rigid body) serves as a control group. The structural characterization can properly describe the structural responses under the wave loading (Dermentzoglou et al., 2021). Therefore, the corresponding natural frequency of the first mode for each model is obtained by the analytical solution for a cantilever beam,  $f_n = \frac{k_n}{2\pi} \sqrt{\frac{EI}{\rho_s l^4}}$ , where  $k_n = 3.52$  (Young et al., 2012). The range of wave conditions modeled is given in Table 1 with a constant wave height  $H = 0.04$  m, water depth  $h = 0.3$  m, and a series of wave periods  $T = 0.6$ -1.6 s. The incident wave ranges from Stokes 2nd order to Stokes 3rd order before reaching the wall according to Le Méhauté (2013).

**Table 1**  
Structural and wave properties in the present simulations.

Model	Mechanical properties					$H$ (m)	$T$ (s)
	$\rho_s$ (kg/m <sup>3</sup> )	$E$ (GPa)	$f_n$ (Hz)	$\gamma$	$\beta$		
1	1200	0.0120	2.640	0.08	0.10	0.04	0.6-1.6*
2	1200	0.0180	3.234	0.08	0.15		
3	1200	0.0240	3.734	0.08	0.20		
4	1200	0.0300	4.175	0.08	0.25		
5	1200	0.0360	4.573	0.08	0.30		
6	1200	0.0480	5.281	0.08	0.40		
7	1200	0.0720	6.468	0.08	0.60		
8	1200	0.1190	8.315	0.08	1.00		
9	1200	0.5950	18.592	0.08	5.00		
10	1800	35.760	117.687	0.12	30.0		

\* Here the interval of the wave period is 0.2 s.

The boundary conditions are set as follows. In the fluid domain, the left and right sides of the flume are specified as wave inlet and wave outlet, respectively. Wave generation boundary with active wave absorption is applied at the wave inlet and waves are generated by the stream function theory (Fenton, 1988). Wave absorption boundary is applied at the wave outlet and the radiated waves stimulated by the oscillation of the wall can be effectively absorbed at the end of the numerical flume (for more details, see Higuera et al. (2013)). Note that we initially attempted to employ waves2Foam with the relaxation zone approach developed by Jacobsen et al. (2012) for the wave generation and absorption (as that has been used in Li et al. (2018)

231 and Li et al. (2020) for rigid structures). However, our generated wave height  
 232 could not reach the targeted value during propagation with mesh deforma-  
 233 tion. Instead, we incorporated the wave generation and absorption technique  
 234 in IHFOAM (using active wave absorption to cancel out the reached waves  
 235 on the boundaries) and were able to achieve accurate and stable wave propa-  
 236 gation when combined with moving mesh. The bottom and the top are set as  
 237 no-slip wall and atmospheric boundary conditions, respectively. The inter-  
 238 faces with solid are set as the Dirichlet boundary condition for the velocity  
 239 (see Eq. 11). In the solid domain, the interfaces with fluid are specified as  
 240 the Neumann boundary condition for the traction (see Eq. 10). The bottom  
 241 of the wall is set as a fixed-support boundary condition and keeps clamped  
 242 under the wave loading.

243 The present fully-coupled model is based on a cell-centered finite volume  
 244 method. Spatial and temporal discretizations are introduced in the compu-  
 245 tational simulation with a non-overlapping structured hexahedral mesh and  
 246 finite time steps. In particular, the spatial domain consists of the fluid sub-  
 247 domain and the solid sub-domain, which can simultaneously represent the  
 248 evolution of the fluid and the structure. The governing equations (Eq. 1 and  
 249 Eq. 2) can be numerically solved using specified initial and boundary condi-  
 250 tions. The Pressure Implicit with Splitting of Operators (PISO) algorithm  
 251 (Issa, 1986) is applied to decouple the  $p$ - $\mathbf{u}$  equations and iteratively solve  
 252 them. Time integration is determined by the Courant-Friedrichs-Lewy (CFL)  
 253 criteria. The simulations are performed with a fixed time step  $\Delta t = 0.001$  s,  
 254 which ensures the Courant number  $Co \leq 0.1$  for wave propagation and  
 255  $Co \leq 0.2$  near the structure as the wave orbital velocity increases due to  
 256 the reflection. The passage of 30 waves per simulation case takes approx-  
 257 imately 2 days using 12 processors on the supercomputer of the National  
 258 Supercomputing Centre (NSCC).

## 259 4. Model verification

### 260 4.1. Verification against solitary wave impacting on an elastic wall

261 Detailed validations for the present model have been conducted in Huang  
 262 and Li (2022) for an elastic submerged horizontal plate in nonlinear waves.  
 263 For the present study involving a vertical elastic wall in periodic waves, there  
 264 was no experimental study in the open literature. The present model was  
 265 thereby adequately verified against the numerical results of He and Kashiwagi  
 266 (2012), who investigated the hydroelastic behavior of a vertical cantilever

267 wall in a solitary wave. Their work was well validated against the analytical  
 268 result of Peter and Meylan (2010) and another numerical simulation based on  
 269 a mode-expansion method (He and Kashiwagi, 2009). Recently, their results  
 270 were also verified by Akrish et al. (2018). Therefore, their model results are  
 271 seeming to be reliable for our verification purposes.

272 In this subsection, the case of the top-free wall was simulated with differ-  
 273 ent cell sizes for the fluid domain and the solid domain. A solitary wave with  
 274 a wave height of  $0.04h$  was generated at  $x = -50h$ . The mass coefficient  
 275  $\gamma$  and the stiffness coefficient  $\beta$  of the wall are 0.01 and 0.04, respectively.  
 276 The height of the wall is  $1.1h$  and the normalized time duration  $t\sqrt{g/h}$  is  
 277 180 in this verification simulation, in which the water depth is again set as  
 278  $h = 0.3$  m. For comparison, the wave elevation  $\eta/H$  at  $x = -10h$  and the  
 279 horizontal displacement  $D_x/H$  of the wall at  $z = h/2$  were recorded.

280 Three sets of mesh with 5, 10, and 15 cells per wave height were em-  
 281 ployed. The aspect ratio of the cells was set as  $1/3$  (i.e., cell height/cell  
 282 width), which conformed to the range proposed in Jacobsen et al. (2014).  
 283 The simulated results show good agreement with He and Kashiwagi (2012)  
 284 as seen in Fig. 3a. A small drop in our simulated reflected wave occurs at  
 285  $t\sqrt{g/h} = 132.8$ . It is because the deformation of the wall transfers the wave  
 286 energy downstream, which is not considered in He and Kashiwagi (2012).  
 287 It is found that the result of 10 cells/ $H$  is almost identical to that of 15  
 288 cells/ $H$ , while the result of 5 cells/ $H$  slightly overestimates the wave eleva-  
 289 tion. Therefore, the mesh set with 10 cells per wave height is adopted for  
 290 what follows in this subsection. The horizontal displacement of the wall at  
 291  $z = h/2$  is verified using three different sets of solid mesh with 200, 400, and  
 292 600 cells (i.e.,  $2 \times 100$ ,  $4 \times 100$ , and  $6 \times 100$  cells in the horizontal and vertical  
 293 directions). In Fig. 3b, the result of 400 cells is fairly close to that of 600  
 294 cells, which achieves convergence. However, the displacement of 200 cells is  
 295 notably lower, especially near the peak value. The mesh set of 400 cells is  
 296 seen to provide an accurate and efficient solution, therefore is used for the  
 297 solid domain in the following simulations.

#### 298 4.2. Validation against periodic waves impacting on a rigid wall

299 Subsection 4.1 provided the verification on a solitary wave. As the present  
 300 study focuses on the periodic waves, the numerical model was validated  
 301 against the experiment of Didier et al. (2014) for regular waves impacting  
 302 on a vertical rigid wall. The numerical simulations were conducted with the  
 303 identical setup as in Didier et al. (2014). A non-breaking wave case with

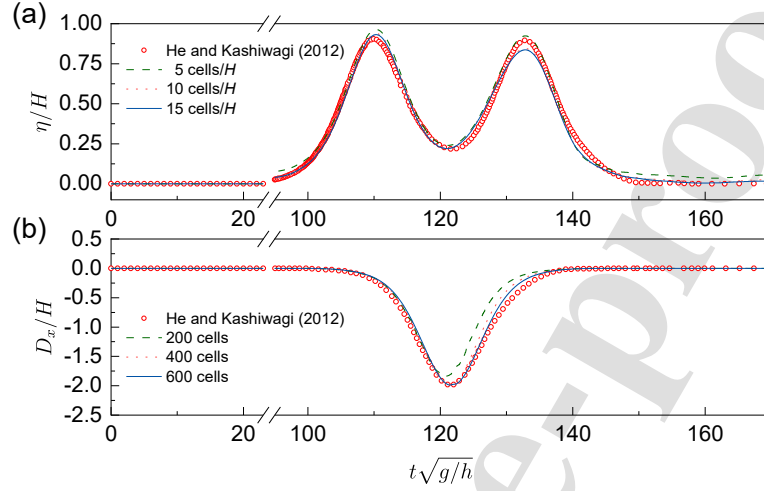


**Fig. 3.** Comparison of the normalized (a) wave elevation at  $x = -10h$  and (b) horizontal displacement of the wall at  $z = h/2$  between the present simulation and He and Kashiwagi (2012).

304  $H = 0.1$  m,  $T = 1.3$  s, and  $h = 0.325$  m was selected for the present valida-  
 305 tion. Three densities of mesh (i.e., 10, 15, and 20 cells per wave height with  
 306 an aspect ratio of 1/3) were tested for the grid convergence study. Fig. 4a  
 307 shows the comparison of the wave elevation at 2.643 m from the wave-maker  
 308 initial position. All sets of the mesh give satisfactory predictions compared to  
 309 the laboratory measurement. The mesh of 15 cells/ $H$  shows nearly identical  
 310 results as the mesh of 20 cells/ $H$  and slightly more accurate results com-  
 311 pared to the mesh of 10 cells/ $H$ . Fig. 4(b-c) show the pressure at 0.055 m  
 312 and 0.165 m above the bottom of the wall, respectively. A good agreement  
 313 is globally observed between numerical and experimental results. Note that  
 314 the maximum pressure in the simulation is larger than the experiment, which  
 315 is due to an insufficient data sampling rate at the experimental tests, as re-  
 316 ported in Didier et al. (2014). Based on the above results, the mesh set with  
 317 15 cells per wave height is used for the following simulations. The utilized  
 318 final mesh with a zoom-in view is shown in Fig. 5, where the fluid inter-  
 319 face is conformal to the solid interface to minimize the interpolation error at  
 320 boundaries.

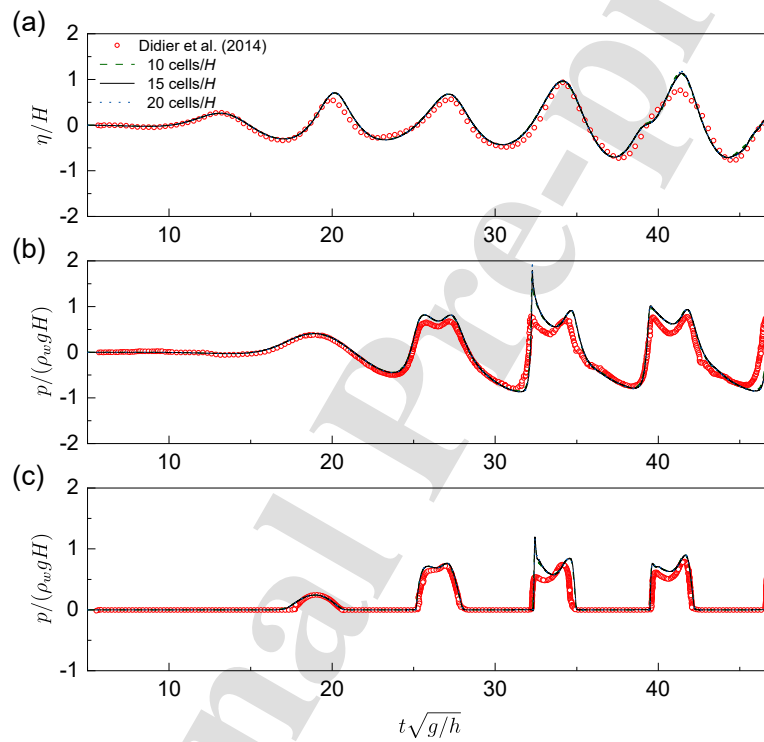


**Fig. 4.** Comparison of the normalized (a) wave elevation at 2.643 m from the wave-maker initial position, (b) pressure at 0.055 m above the bottom of the wall, and (c) pressure at 0.165 m above the bottom of the wall.

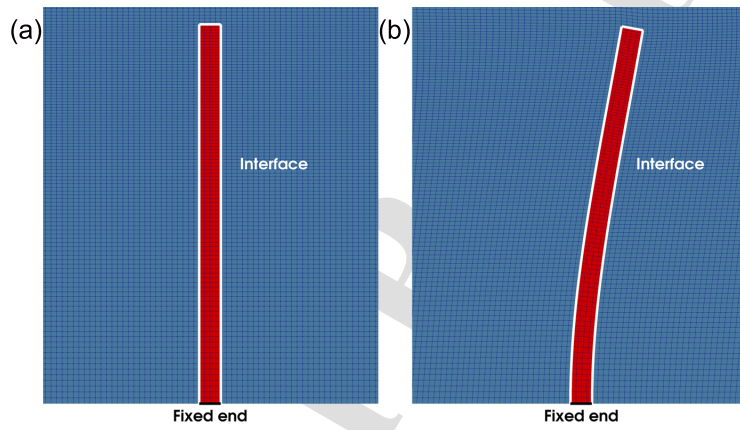


**Fig. 5.** The zoom-in view of the (a) undeformed and (b) deformed mesh with blue denoting the fluid domain and red denoting the solid domain. The white line represents the interface between the fluid and solid, and the black line at the bottom represents the fixed end of the wall.



## 321 5. Results and discussion

322 Detailed investigations of waves interacting with an elastic wall in terms  
 323 of hydrodynamic characteristics, structural dynamic responses, structural  
 324 optimization, and material damping effect are presented in the following  
 325 subsections.

### 326 5.1. Hydrodynamic characteristics

#### 327 5.1.1. Reflection and transmission coefficients

328 To investigate the energy propagation of waves interacting with the elastic  
 329 wall, the reflection coefficient ( $C_r$ , i.e., the ratio of the reflected wave height  
 330 to the incident wave height) and the transmission coefficient ( $C_t$ , i.e., the  
 331 ratio of the radiated wave height caused by the oscillation of the wall to  
 332 the incident wave height) against the stiffness coefficient  $\beta$  are analyzed and  
 333 shown in Fig. 6. The rigid wall (i.e.,  $\beta = 30$ ) presents a perfect reflection  
 334 with no transmission despite the changes in wave steepness ( $H/L$ ). For the  
 335 elastic walls, as  $\beta$  increases from 0.10 to 5,  $C_r$  gradually increases whilst  $C_t$   
 336 decreases. This trend is more obvious when the value of  $\beta$  is relatively small.  
 337 Besides, it is seen that  $C_r$  is with an increasing tendency against the increase  
 338 of the wavelength  $L$  (corresponding to the decrease of  $H/L$ ), especially for  
 339 the smaller  $\beta$ , indicating that longer waves are easier to be reflected by elastic  
 340 walls. It is worthwhile to mention that the value of  $C_r^2 + C_t^2$  is close to 1 for all  
 341 scenarios, which implies that the total reflected and transmitted wave energy  
 342 is approximately equal to the incident wave energy with negligible energy  
 343 dissipation. Thereby, the increase of  $C_r$  naturally leads to the decrease of  $C_t$   
 344 for each model.

#### 345 5.1.2. Wave run-up and loading

346 Besides  $C_r$  and  $C_t$ , other important considerations are the wave run-up  
 347 and loading on the wall with various stiffness coefficients. The wave run-  
 348 up  $R$  (nondimensionalized by  $H$ ) and the horizontal peak force per unit  
 349 width  $F_{x,max}$  (nondimensionalized by  $\rho_w g h H$ ) exerted on the wall are shown  
 350 in Fig. 7. For both the rigid and elastic walls, the normalized wave run-  
 351 up  $R/H$  increases with the wavelength  $L$ , as illustrated in Fig. 7a. This  
 352 is because the longer waves have larger wave excursion,  $A_w = u_{x,max} T / 2\pi$ ,  
 353 where  $u_{x,max}$  is the maximum horizontal velocity of the fluid particle.  $A_w$   
 354 increases from 0.020 m to 0.036 m as the wavelength  $L$  increases from 0.56 m  
 355 to 2.53 m (corresponding to  $H/L$  decreases from 0.071 to 0.016). Besides,

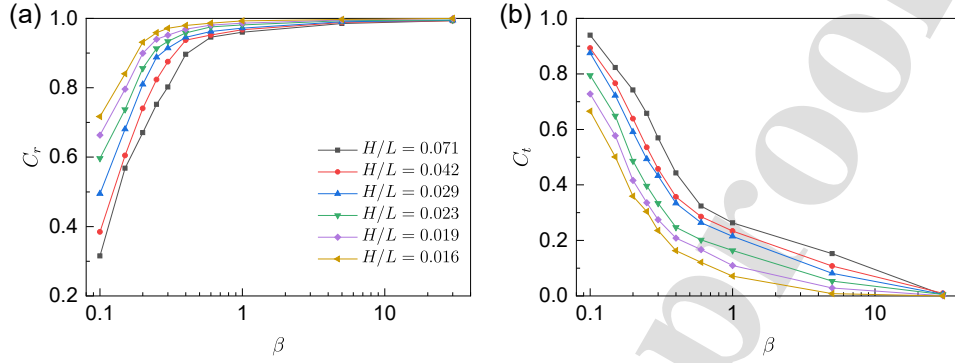


**Fig. 6.** Comparisons of (a) reflection coefficient and (b) transmission coefficient induced by walls with different stiffness coefficients  $\beta$ .

356  $R/H$  gradually increases with  $\beta$  and the gradient is negligible when  $\beta > 1$ ,  
 357 which is similar to the tendency of  $C_r$ . Fig. 7b shows that the normalized  
 358  $F_{x,max}$  also increases with  $\beta$  and  $L$ , while the change of the wavelength makes  
 359 a bigger difference of  $F_{x,max}$  especially for the rigid wall. The increases of both  
 360 the wave run-up and loading against  $\beta$  are due to the enhanced wave reflection  
 361 causing a higher wave elevation on the wall when superimposed with the  
 362 incident wave. Therefore, the dynamic pressure on the wall can be increased  
 363 with the wave reflection, which causes a higher pressure difference between  
 364 the front and back of the wall. Compared with the rigid wall, the introduction  
 365 of flexibility can significantly reduce the wave run-up and loading on the wall.

366 The predictions of the wave run-up and horizontal peak force are of great  
 367 importance for the design and optimization of flexible structures in coastal  
 368 engineering. Previous studies showed a linear dependence of the normalized  
 369 run-up on the wave steepness (Hunt, 1959):

$$\frac{R_{pred}}{H} = a \left( \frac{H}{L} \right)^c \quad (15)$$

370 For the wave run-up estimation on vertical elastic structures, the stiffness  
 371 coefficient  $\beta$  describing the flexural rigidity should also be considered in ad-  
 372 dition to the wave steepness. Therefore, we propose a modified equation for

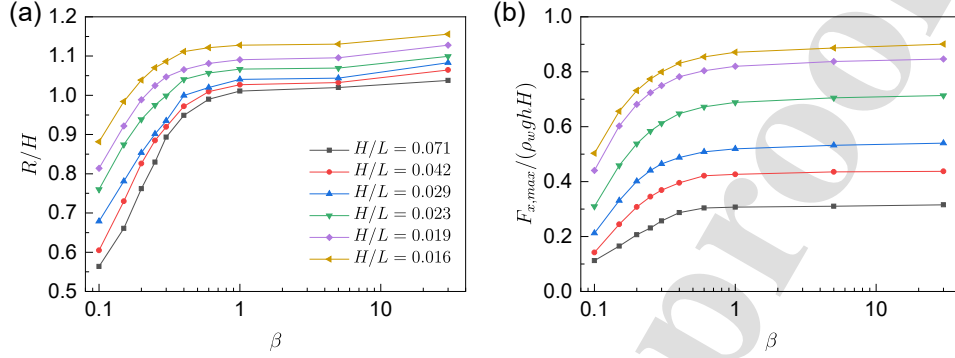


**Fig. 7.** Comparisons of (a) wave run-up and (b) horizontal peak wave force between walls with different stiffness coefficients  $\beta$ .

373 the prediction of the wave run-up on a vertical elastic wall as follows:

$$\frac{R_{pred}}{H} = a \left( \frac{1}{1 + \frac{1}{k\beta}} \right) \left( \frac{H}{L} \right)^c \quad (16)$$

374 where  $R_{pred}$  is the predicted wave run-up,  $a$ ,  $k$ , and  $c$  are the empirical  
 375 coefficients. This form of the formula allows it to revert to that for rigid  
 376 structures (Eq. 15) when  $\beta$  is very large. A wide range of wall stiffness  
 377 and wave conditions are calibrated in Fig. 8a for the best fitting, resulting  
 378 in  $a = 0.697$ ,  $k = 20.629$ , and  $c = -0.132$ . The empirical formula (Eq. 16)  
 379 successfully captures the numerical results with a coefficient of determination  
 380 of 0.894. Most of the cases lie within  $\pm 6\%$  deviations. Likewise, the predicted  
 381 horizontal peak force exerted on the wall per unit width  $F_{x,max,pred}$  can be  
 382 obtained by:

$$\frac{F_{x,max,pred}}{\rho_w g h H} = a \left( \frac{1}{1 + \frac{1}{k\beta}} \right) \left( \frac{H}{L} \right)^c \quad (17)$$

383 Forces calculated by Eq. 17 with  $a = 0.033$ ,  $k = 12.799$ , and  $c = -0.815$  are  
 384 compared with numerical results in Fig. 8b. It provides good estimations with  
 385 a coefficient of determination of 0.962. These modified prediction formulae  
 386 can provide the evaluations for the wave run-up and loading of vertical elastic  
 387 structures.

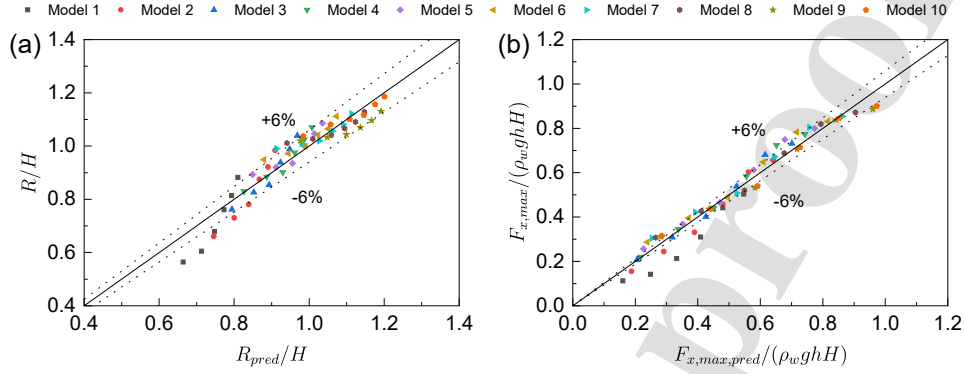


**Fig. 8.** Comparisons of the predicted (a) wave run-up obtained by Eq. 16 and (b) horizontal peak wave force obtained by Eq. 17 with numerical results.

## 388 5.2. Dynamic response of the wall

### 389 5.2.1. Displacement of the wall

390 To further investigate the structural response of the elastic wall in peri-  
 391 odic waves, the horizontal displacement of the wall is analyzed. Fig. 9 shows  
 392 the comparisons between the wave elevation  $\eta$  at the front face of the moving  
 393 wall, horizontal wave force  $F_x$ , and the horizontal displacement at the free  
 394 top  $D_x$  during two wave cycles with  $H/L = 0.016$ . For Model 2 (see Fig. 9a),  
 395 an approximately  $0.06T$  phase lag is observed between  $D_x$  and  $\eta$ . Thereby  
 396  $D_x$  slightly lags behind the wave force. Note that the amplitudes of the crest  
 397 and trough are slightly asymmetric for  $\eta$ ,  $F_x$ , and  $D_x$  because of the super-  
 398 position of higher-order nonlinear wave components. In Fig. 9b, the signals  
 399 in the time domain are decomposed into the components of the fundamen-  
 400 tal frequency and higher harmonics using a fast Fourier transform (FFT),  
 401 where the frequencies are normalized by the incident wave frequency ( $f_w$ ).  
 402 It is observed that  $D_x$  has the same frequency as that of the incident wave  
 403 loading. Besides, the amplitude of  $D_x$  is predominant at the fundamental  
 404 frequency, with a minor role in the 2nd harmonic, and negligible in the 3rd  
 405 and 4th harmonics, which is determined by the wave excitation. Fig. 9(c-d)  
 406 present the results of Model 5 in the same wave condition. With a larger  $\beta$ ,  
 407 the abovementioned phase lag between  $D_x$  and  $\eta$  tends to decrease to about  
 408  $0.02T$ , which implies the wall displacement becomes more synchronous with  
 409 the exerted wave elevation as well as the wave loading. As expected, the  
 410 vibration frequency is again the same as the wave force, independent of the

411 wall properties.

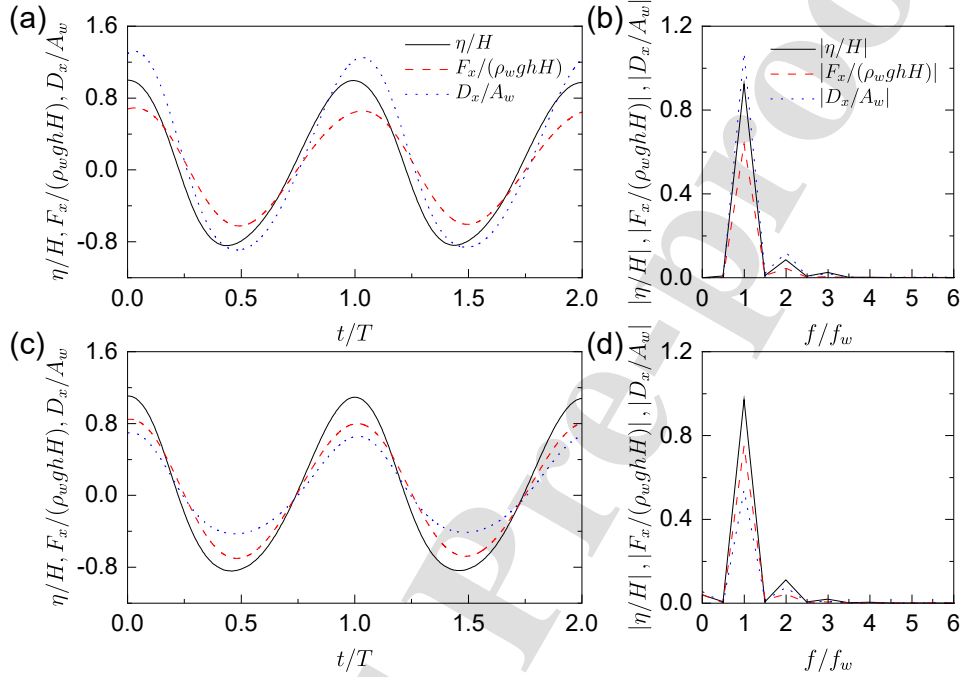


**Fig. 9.** Time series and the corresponding amplitude spectrum of the wave elevation, horizontal wave force, and horizontal displacement of the wall for (a-b) Model 2 and (c-d) Model 5 in waves with  $H/L = 0.016$ .

412 Fig. 10a presents the horizontal maximum displacement  $D_{x,max}$  (nondi-  
 413 mensionalized by the wave excursion  $A_w$ ) against the ratio of the incident  
 414 wave frequency to the natural frequency of the wall,  $f_w/f_n$ . It is obvious  
 415 that  $D_{x,max}/A_w$  rapidly increases with  $f_w/f_n$  under the same wave condi-  
 416 tion. This increase is more significant for waves with a smaller  $H/L$  and  
 417 the structure with a larger  $f_w/f_n$ . However, for the same structure (con-  
 418 nected by dotted lines), a peak of  $D_{x,max}/A_w$  seems to appear at waves with  
 419  $H/L = 0.019$ . Given the same dimensionless parameters as that in Eq. 16  
 420 and Eq. 17, the predicted horizontal maximum displacement  $D_{x,max,pred}$  can  
 421 be directly obtained by the following formula:

$$\frac{D_{x,max,pred}}{A_w} = a \left( \frac{1}{1 + k\beta} \right) \left( \frac{H}{L} \right)^c \quad (18)$$

422 As shown in Fig. 10b,  $D_{x,max,pred}$  predicted by Eq. 18 with  $a = 1.872$ ,  
 423  $k = 17.210$ , and  $c = -0.221$  almost coincide with the numerical results  
 424 with a coefficient of determination of 0.984. Most of the data lie within  
 425 the  $\pm 6\%$  derivations. Therefore, the proposed empirical formula can provide  
 426 satisfactory estimations for the displacement of the elastic wall in a certain  
 range of wave conditions and material stiffness.

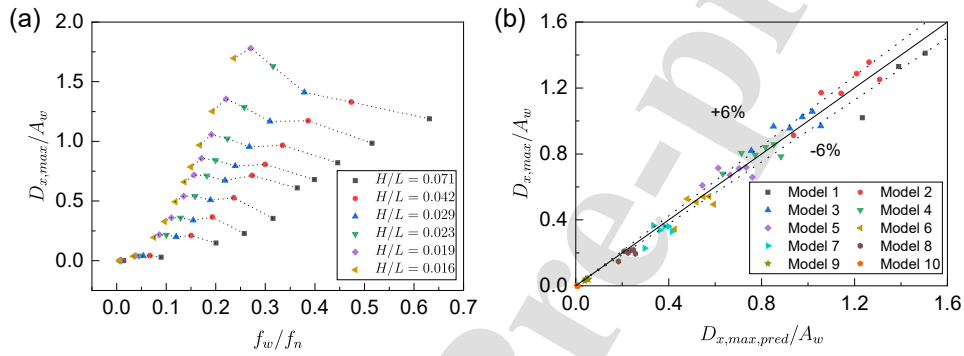


**Fig. 10.** Comparison of the horizontal maximum displacement between (a) cases with different frequency ratios and (b) the predicted and numerical results.

427

### 428 5.2.2. Von Mises stress in the wall

429 Figs. 11-13 present snapshots of the free surface (denoted by blue con-  
 430 tours) together with the bending deflection as well as the von Mises stress  $\sigma_v$   
 431 (nondimensionalized by  $\rho_w g H$ ) in the wall under wave loading. For Model 1  
 432 in periodic waves with  $H/L = 0.029$  and  $f_w/f_n = 0.379$ , a phase lag is seen  
 433 between the structural displacement and the wave elevation, i.e., the horizon-  
 434 tal maximum displacement  $D_{x,max}$  (i.e., shoreward displacement amplitude)  
 435 occurs at  $t = 0.14T$  instead of at the wave crest (see Fig. 11a). At this mo-  
 436 ment, the pressure difference between the upstream and downstream sides  
 437 lead to the peak  $\sigma_v$  during the whole wave cycle. The relatively high stress  
 438 is concentrated near the toe, with a maximum stress  $\sigma_{v,max}$  at the rear side  
 439 of the wall. In the vertical direction,  $\sigma_v$  gradually decreases to zero from the  
 440 bottom to the free top. As waves propagate, the minimum horizontal dis-  
 441 placement  $D_{x,min}$  (i.e., seaward displacement amplitude) of the wall occurs  
 442 at  $t = 0.64T$  (see Fig. 11b).  $\sigma_v$  in Fig. 11b is slightly smaller than that in  
 443 Fig. 11a, which is more obvious at the rear toe of the wall. This is again due

444 to wave nonlinearity, where the fluid moves faster at the wave crest than the  
 445 wave trough (Dean and Dalrymple, 1991).

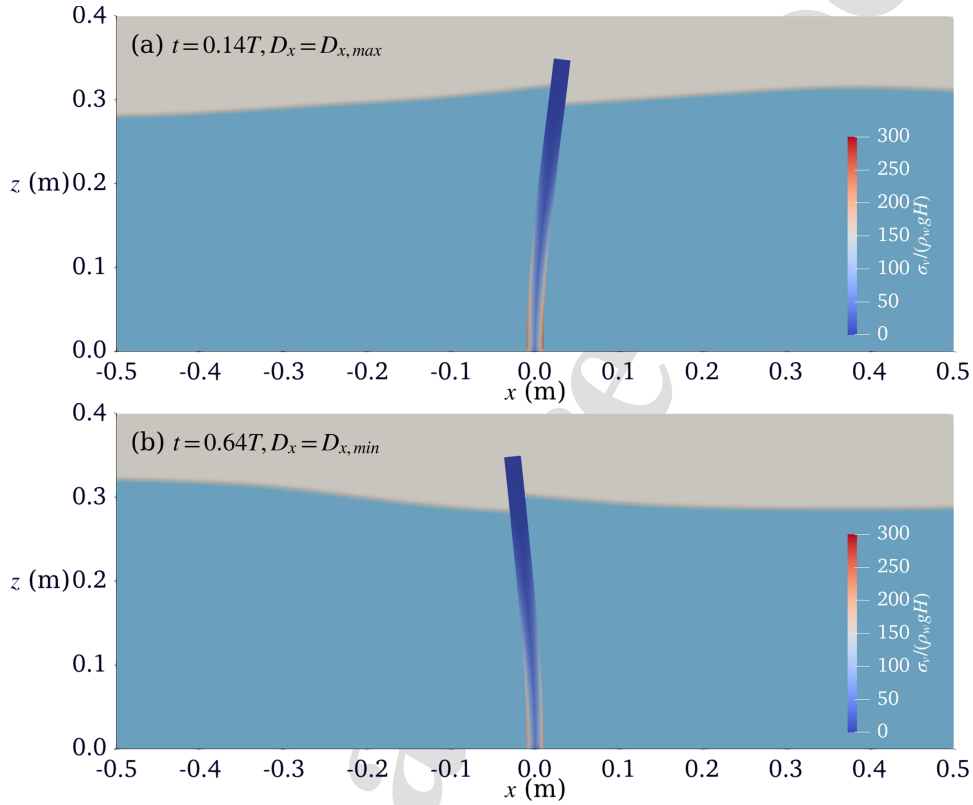


**Fig. 11.** Snapshots of periodic waves with  $H/L = 0.029$  on Model 1 at (a)  $D_x = D_{x,max}$  and (b)  $D_x = D_{x,min}$ .

446 Fig. 12 shows the results of Model 2 with a larger stiffness coefficient.  
 447 Comparing Fig. 12 and Fig. 11, as  $f_w/f_n$  decreases from 0.379 to 0.309,  $\sigma_v$  in  
 448 the wall increases under both wave forth and back loadings, especially near  
 449 the toe of the wall. This is because the restoring force caused by the stiffness  
 450 becomes more dominant compared with the hydrodynamic force. Note that  
 451 the abovementioned phase lag between the wall displacement and the wave  
 452 elevation decreases to about  $0.10T$  with the decrease of  $f_w/f_n$ . Fig. 13 shows  
 453 the results of Model 2 in waves with a smaller  $H/L$ . Comparing Fig. 13  
 454 and Fig. 12, as  $H/L$  decreases from 0.029 to 0.016,  $f_w/f_n$  decreases from

455 0.309 to 0.193. It can be found that the von Mises stress further significantly  
 456 increases. However, the phase lag between  $\eta$  and  $D_x$  decreases to  $0.06T$  with  
 457 the decrease of  $f_w/f_n$ .

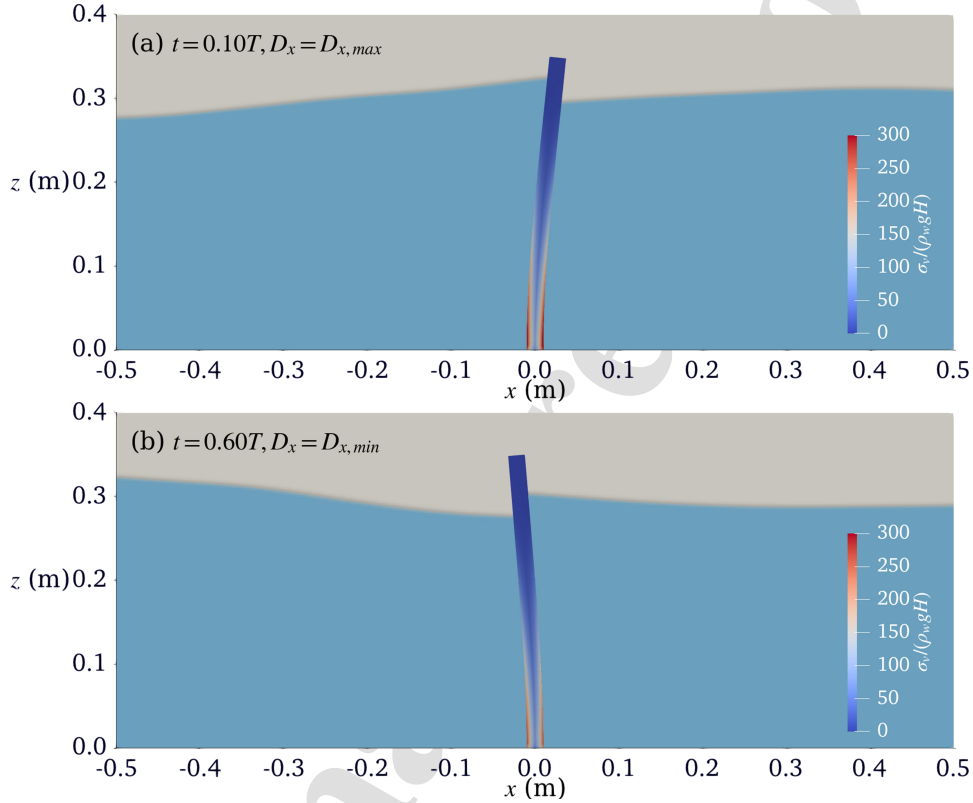


**Fig. 12.** Snapshots of periodic waves with  $H/L = 0.029$  on Model 2 at (a)  $D_x = D_{x,max}$  and (b)  $D_x = D_{x,min}$ .

### 458 5.3. Optimal design conditions of the flexible wall

459 As discussed above, the change of the frequency ratio  $f_w/f_n$  and the wave  
 460 steepness  $H/L$  can significantly affect the wave evolution and the structural  
 461 integrity. A stiffer structure can have larger wave-induced stresses in the wall,  
 462 which has negative impact on the structural integrity. However, the decrease  
 463 of the structural stiffness (i.e., more flexible) can intensify the shoreward  
 464 energy transmission, which can exacerbate coastal vulnerability (Jin et al.,



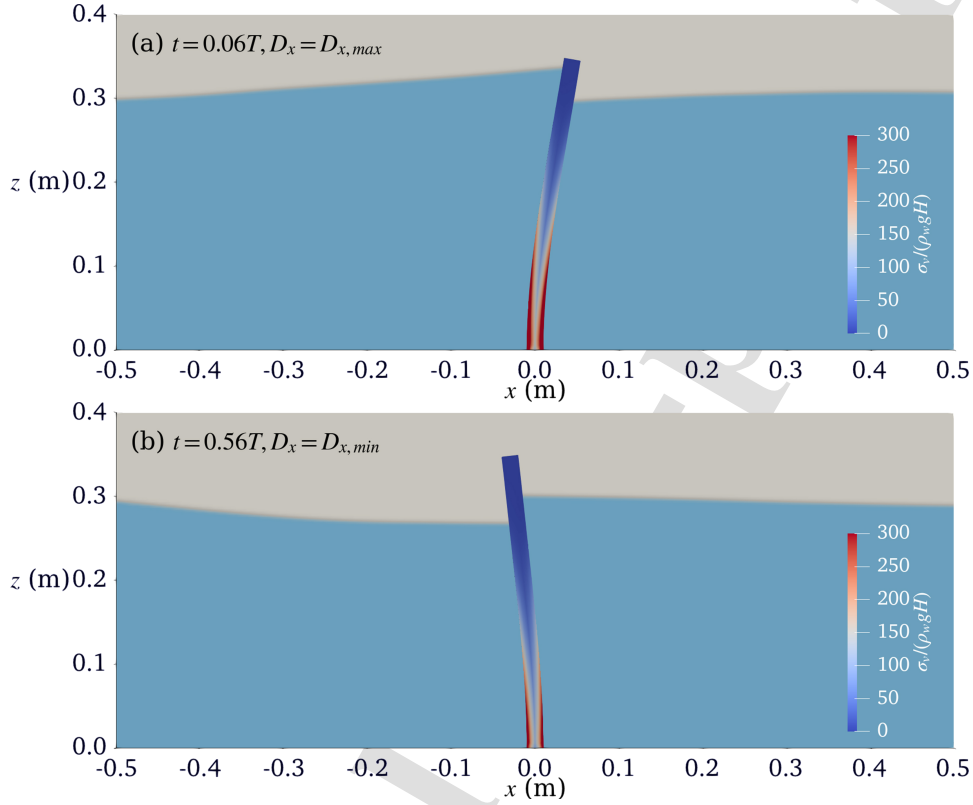


**Fig. 13.** Snapshots of periodic waves with  $H/L = 0.016$  on Model 2 at (a)  $D_x = D_{x,max}$  and (b)  $D_x = D_{x,min}$ .

465 2015). Therefore, a design balance should be considered when incorporating  
 466 the flexibility of the wall. In the present study, a preliminary optimization of  
 467 the flexibility is conducted to balance the defense performance and structural  
 468 integrity.

469 In the optimization, minimizing transmission coefficient  $C_t$  is chosen as  
 470 one objective for improving the defense performance while minimizing max-  
 471 imum von Mises stress  $\sigma_{v,max}$  is another objective for ensuring the integrity  
 472 of the wall. We know from the parametric study above that these two objec-  
 473 tives conflict with each other. Thereby optimal decisions need to be taken  
 474 in the presence of trade-offs between them. Meanwhile, there are also many  
 475 other considerations e.g. the cost, which are not included in the present op-

476 timization scope. Fig. 14a shows the contour of  $C_t$  against  $f_w/f_n$  and  $H/L$ .  
 477 It is seen that the smallest  $C_t$  distributes in the space with small  $f_w/f_n$  and  
 478  $H/L$ . The transmission coefficient seems to be almost uniform for a specific  
 479  $f_w/f_n$ . To ensure low wave transmission ( $C_t < 0.5$ , i.e., 75% energy cut-  
 480 off),  $f_w/f_n < 0.25$  can be an optimal choice. Therefore, we can focus on  
 481 the single objective of minimizing  $\sigma_{v,max}$ . Fig. 14b shows a nearly opposite  
 482 trend of  $\sigma_{v,max}$  against  $f_w/f_n$  and  $H/L$ . It is noted that for relatively longer  
 483 waves ( $0.016 < H/L < 0.029$ ) and smaller frequency ratio ( $f_w/f_n < 0.25$ ),  
 484  $\sigma_{v,max}$  in the wall is extreme large (Fig. 14b). The decrease in wavelength  
 485 (corresponding to the increase of  $H/L$ ) can significantly reduce the stress  
 486 in the structure.  $H/L > 0.029$  results in  $\sigma_{v,max}/\rho_w g H$  almost smaller than  
 487 300, thereby can be considered as an optimal choice for this range of wave  
 488 steepness. Therefore, The area of  $H/L > 0.029$  and  $f_w/f_n < 0.25$  could be  
 489 an optimal choice for design balance. Note that optimal solutions are dependen-  
 490 dent on the relative importance of the objectives, which can lead to different  
 solutions in different applications.

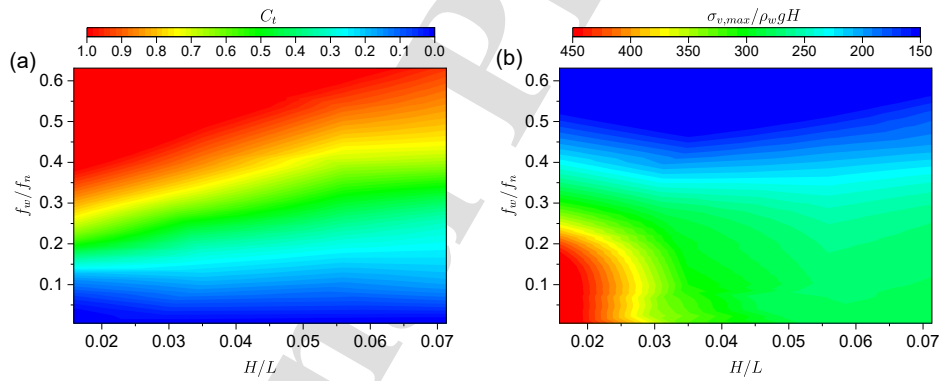


**Fig. 14.** Contours of (a) transmission coefficient and (b) maximum von Mises stress against the ratio frequency and the wave steepness.

491

#### 492 5.4. The effect of the material damping

493 As an effective-damping material, rubbers can restrain the vibratory motion  
 494 by dissipating the energy. As the aforementioned study did not consider  
 495 material damping, in this section, we aim to study how much material damp-  
 496 ing can affect the interaction between periodic waves and an elastic wall.  
 497 To consider the material damping, an additional term (i.e.,  $c_s \int \rho_s \frac{\partial \mathbf{D}}{\partial t} dV$ ) is

498 added at the left hand side of Eq. 6, in which  $c_s$  is the constant viscous  
 499 damping coefficient of the material. An approximate damping coefficient  
 500  $c_s = 0.15 \text{ s}^{-1}$  of rubber is introduced herein with reference to the quantifica-  
 501 tion of Lin et al. (2005).

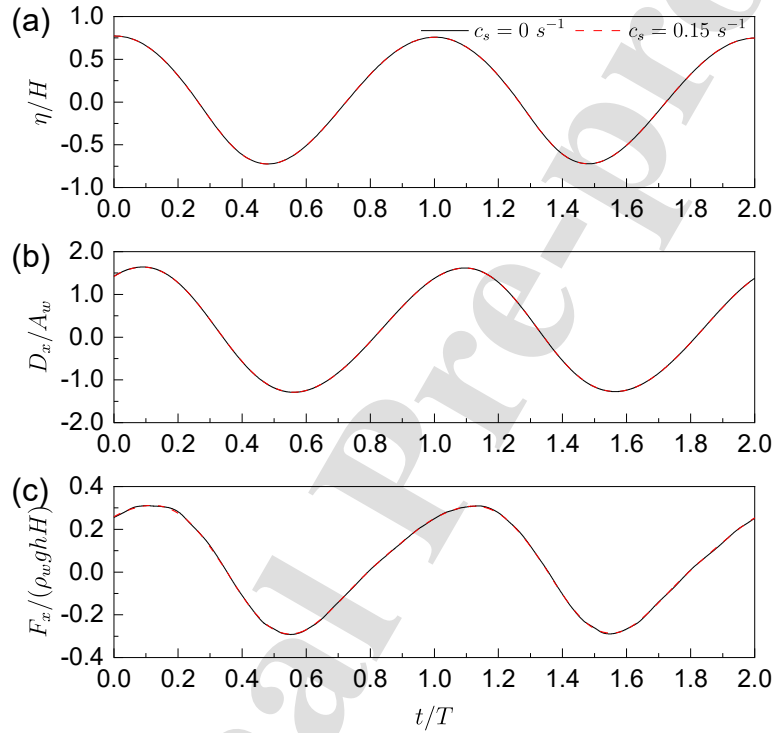


**Fig. 15.** Comparison of the normalized (a) wave elevation, (b) horizontal displacement at the free top, and (c) horizontal force exerted on walls with and without material damping.

502 Here we present the results for Model 1 in waves with  $H/L = 0.023$  as an  
 503 example. The dimensionless wave elevation of WG4, horizontal displacement  
 504 of the free top, and horizontal force per unit width exerted on the wall with  
 505 ( $c_s = 0.15 \text{ s}^{-1}$ ) and without ( $c_s = 0 \text{ s}^{-1}$ ) material damping are compared  
 506 in Fig. 15. It can be found that the two curves coincide with each other in  
 507 all subplots, which indicates that the material damping does not affect the  
 508 hydrodynamic characteristics and structural responses of the elastic wall in  
 509 periodic waves. This is because the loading of ocean waves is continuous

510 and with low frequency. Therefore the damping term is proportional to a  
511 very low deformation rate (i.e., small  $\frac{\partial \mathbf{D}}{\partial t}$ ), resulting in a negligible damping  
512 effect compared to the wave loading. As a result, the material damping can  
513 be ignored in simulations leading to related problems. This corroborates  
514 the discussion given in Huang and Li (2022), in which the authors inferred  
515 that the material damping has negligible influence on the hydroelastic wave-  
516 structure interaction. However, the damping effect for the impact of other  
517 environmental loads, e.g., seismic loads may still need to be considered.

## 518 6. Conclusions

519 The present study performed a systematic investigation of the hydroelas-  
520 tic behavior of a wall in periodic waves using a fully-coupled wave-structure  
521 interaction model. The main conclusions in this study are drawn as follows:

522 (1) In contrast to a rigid wall with perfect reflection, a remarkable reduc-  
523 tion is observed in wave reflection with an increased wave transmission for  
524 the applied elastic wall. This is more obvious for more flexible walls.

525 (2) Higher flexibility of the wall is observed to significantly reduce the  
526 wave run-up and loading. Modified empirical formulae are proposed for the  
527 predictions of run-up and maximum wave loading by introducing the effect  
528 of structural flexibility, which provides quick estimations for the results ob-  
529 tained through time-consuming simulations. This can be particularly useful  
530 in early-stage design processes.

531 (3) A slight phase lag is observed between the horizontal displacement of  
532 the elastic wall and the exerted wave loading. It increases with the ratio of  
533 the incident wave frequency to the wall's natural frequency. The structural  
534 response has the same frequency as that of the wave force. An empirical  
535 formula is also proposed for the prediction of the maximum displacement.

536 (4) The normalized von Mises stress in the wall increases with the decrease  
537 of the ratio of the incident wave frequency to the wall's natural frequency.  
538 The relatively high stresses are concentrated near the toe of the wall, with  
539 maximum stress at the rear toe of the wall. Similar to the wall displacement,  
540 the stress is larger in the shoreward direction than those in the seaward  
541 direction.

542 (5) The optimization of the flexible wall is studied taking into account  
543 both the defense performance and the structural integrity. Besides, material  
544 damping is proved to have a negligible effect on the interaction between  
545 periodic waves and an elastic wall.

546 The present work aims to support the design and optimization of an elas-  
547 tic wall interacting with periodic waves. More experimental data are required  
548 to fully validate the design and optimizations. Meanwhile, the present model  
549 (released in the next section) should be a useful tool for predicting the interac-  
550 tion between ocean waves and flexible structures in the coastal and offshore  
551 regions.

### 552 **Availability of source codes**

553 The source code implemented and utilized in the present work is publicly  
554 available at: <https://github.com/huzhengyu/wave2solids>. The fully-coupled  
555 wave-structure interaction code is developed in OpenFOAM version foam-  
556 extend-4.0. The present simulation for the elastic wall in periodic waves is  
557 provided as a tutorial.

### 558 **Acknowledgment**

559 This study was supported in part with computational resources provided  
560 by the National Supercomputing Centre, Singapore (<https://www.nsc.sg>),  
561 under Project ID: 11002459.

### **References**

- Akrish, G., Rabinovitch, O., Agnon, Y., 2018. Hydroelasticity and nonlin-  
earity in the interaction between water waves and an elastic wall. *Journal  
of Fluid Mechanics* 845, 293–320. <https://doi.org/10.1017/jfm.2018.207>.
- Attili, T., Heller, V., Triantafyllou, S., 2021. A numerical investiga-  
tion of tsunamis impacting dams. *Coastal Engineering*. 169, 103942.  
<https://doi.org/10.1016/j.coastaleng.2021.103942>.
- Cardiff, P., Karač, A., De Jaeger, P., Jasak, H., Nagy, J., Ivanković, A.,  
Tuković, Ž., 2018. An open-source finite volume toolbox for solid mechanics  
and fluid-solid interaction simulations. arXiv preprint arXiv:1808.10736 .
- Dean, R.G., Dalrymple, R.A., 1991. *Water wave mechanics for engineers and  
scientists*. volume 2. world scientific publishing company.

- Dermentzoglou, D., Castellino, M., De Girolamo, P., Partovi, M., Schrepers, G.J., Antonini, A., 2021. Crownwall failure analysis through finite element method. *Journal of Marine Science and Engineering* 9, 35. <https://doi.org/10.3390/jmse9010035>.
- Didier, E., Neves, D., Martins, R., Neves, M., 2014. Wave interaction with a vertical wall: Sph numerical and experimental modeling. *Ocean Engineering* 88, 330–341. <https://doi.org/10.1016/j.oceaneng.2014.06.029>.
- Fenton, J.D., 1988. The numerical solution of steady water wave problems. *Computers & Geosciences* 14, 357–368. [https://doi.org/10.1016/0098-3004\(88\)90066-0](https://doi.org/10.1016/0098-3004(88)90066-0).
- Field, C.B., Barros, V.R., 2014. *Climate change 2014–Impacts, adaptation and vulnerability: Regional aspects*. Cambridge University Press.
- Goda, Y., Suzuki, Y., 1977. Estimation of incident and reflected waves in random wave experiments, in: *Proceedings of the 15th International Conference on Coastal Engineering ASCE1976*, pp. 828–845. <https://doi.org/10.1061/9780872620834.048>.
- He, G., Kashiwagi, M., 2009. Nonlinear solution for vibration of vertical plate and transient waves generated by wave impact. *International Journal of Offshore and Polar Engineering* 19.
- He, G., Kashiwagi, M., 2012. Numerical analysis of the hydroelastic behavior of a vertical plate due to solitary waves. *Journal of Marine Science and Technology*. 17, 154–167. <https://doi.org/10.1007/s00773-011-0155-9>.
- Higuera, P., Lara, J.L., Losada, I.J., 2013. Realistic wave generation and active wave absorption for navier–stokes models: Application to openfoam®. *Coastal Engineering* 71, 102–118. <https://doi.org/10.1016/j.coastaleng.2012.07.002>.
- Hirt, C.W., Nichols, B.D., 1981. Volume of fluid (vof) method for the dynamics of free boundaries. *Journal of Computational Physics*. 39, 201–225. [https://doi.org/10.1016/0021-9991\(81\)90145-5](https://doi.org/10.1016/0021-9991(81)90145-5).
- Hsiao, S.C., Lin, T.C., 2010. Tsunami-like solitary waves impinging and overtopping an impermeable seawall: Experiment and rans modeling. *Coastal Engineering* 57, 1–18. <https://doi.org/10.1016/j.coastaleng.2009.08.004>.

- Huang, L., Li, Y., 2022. Design of the submerged horizontal plate breakwater using a fully coupled hydroelastic approach. *Computer-Aided Civil and Infrastructure Engineering* 37, 915–932. <https://doi.org/10.1111/mice.12784>.
- Huang, L., Li, Y., Benites-Munoz, D., Windt, C.W., Feichtner, A., Tavakoli, S., Davidson, J., Paredes, R., Quintana, T., Ransley, E., Colombo, M., Li, M., Cardiff, P., Tabor, G., 2022. A review on the modelling of wave-structure interactions based on openfoam. *OpenFOAM® Journal* 2, 116–142. <https://doi.org/10.51560/ofj.v2.65>.
- Huang, L., Ren, K., Li, M., Tuković, Ž., Cardiff, P., Thomas, G., 2019. Fluid-structure interaction of a large ice sheet in waves. *Ocean Engineering* 182, 102–111. <https://doi.org/10.1016/j.oceaneng.2019.04.015>.
- Hunt, I.A., 1959. Design of seawalls and breakwaters. *Journal of the Waterways and Harbors Division* 85, 123–152. <https://doi.org/doi:10.1061/JWHEAU.0000129>.
- Issa, R.I., 1986. Solution of the implicitly discretised fluid flow equations by operator-splitting. *Journal of Computational Physics* 62, 40–65. [https://doi.org/10.1016/0021-9991\(86\)90099-9](https://doi.org/10.1016/0021-9991(86)90099-9).
- Jacobsen, N.G., Fredsoe, J., Jensen, J.H., 2014. Formation and development of a breaker bar under regular waves. part 1: Model description and hydrodynamics. *Coastal Engineering* 88, 182–193. <https://doi.org/10.1016/j.coastaleng.2013.12.008>.
- Jacobsen, N.G., Fuhrman, D.R., Fredsøe, J., 2012. A wave generation toolbox for the open-source cfd library: Openfoam®. *International Journal for Numerical Methods in Fluids* 70, 1073–1088. <https://doi.org/10.1002/flid.2726>.
- Jin, D., Hoagland, P., Au, D.K., Qiu, J., 2015. Shoreline change, seawalls, and coastal property values. *Ocean & Coastal Management* 114, 185–193. <https://doi.org/10.1016/j.ocecoaman.2015.06.025>.
- Kumar, G.M., Sriram, V., 2020. Development of a hybrid model based on mesh and meshfree methods and its application to fluid–elastic structure interaction for free surface waves. *Journal of Fluids and Structures* 99. <https://doi.org/10.1016/j.jfluidstructs.2020.103159>.

- Le Méhauté, B., 2013. An introduction to hydrodynamics and water waves. Springer Science & Business Media.
- Li, Y., Ong, M.C., Gudmestad, O.T., Hjertager, B.H., 2020. The effects of slab geometries and wave directions on the steep wave-induced soil response and liquefaction around gravity-based offshore foundations. *Ships and Offshore Structures* 15, 866–877. 10.1080/17445302.2019.1690736. doi: 10.1080/17445302.2019.1690736.
- Li, Y., Ong, M.C., Tang, T., 2018. Numerical analysis of wave-induced poro-elastic seabed response around a hexagonal gravity-based offshore foundation. *Coastal Engineering* 136, 81–95. <https://doi.org/10.1016/j.coastaleng.2018.02.005>.
- Liao, K., Hu, C., 2013. A coupled fdm–fem method for free surface flow interaction with thin elastic plate. *Journal of Marine Science and Technology* 18, 1–11. <https://doi.org/10.1007/s00773-012-0191-0>.
- Lin, T.R., Farag, N.H., Pan, J., 2005. Evaluation of frequency dependent rubber mount stiffness and damping by impact test. *Applied Acoustics* 66, 829–844. <https://doi.org/10.1016/j.apacoust.2004.10.004>.
- Nicholls, R.J., Cazenave, A., 2010. Sea-level rise and its impact on coastal zones. *Science* 328, 1517–1520. <https://doi.org/10.1126/science.1185782>.
- Ning, D., Wang, R., Chen, L., Li, J., Zang, J., Cheng, L., Liu, S., 2017. Extreme wave run-up and pressure on a vertical seawall. *Applied Ocean Research* 67, 188–200. <https://doi.org/10.1016/j.apor.2017.07.015>.
- Peter, M.A., Meylan, M.H., 2010. A general spectral approach to the time-domain evolution of linear water waves impacting on a vertical elastic plate. *SIAM Journal on Applied Mathematics* 70, 2308–2328. <https://doi.org/10.1137/090756557>.
- Ranasinghe, R., 2016. Assessing climate change impacts on open sandy coasts: A review. *Earth-Science Reviews* 160, 320–332. <https://doi.org/10.1016/j.earscirev.2016.07.011>.
- Reeve, D.E., Soliman, A., Lin, P.Z., 2008. Numerical study of combined overflow and wave overtopping over a smooth impermeable seawall. *Coastal Engineering* 55, 155–166. <https://doi.org/10.1016/j.coastaleng.2007.09.008>.



- Sree, D.K.K., Mandal, S., Law, A.W.K., 2021. Surface wave interactions with submerged horizontal viscoelastic sheets. *Applied Ocean Research* 107. <https://doi.org/10.1016/j.apor.2020.102483>.
- Sriram, V., Ma, Q.W., 2012. Improved MLPG-R method for simulating 2d interaction between violent waves and elastic structures. *Journal of Computational Physics* 231, 7650–7670. <https://doi.org/10.1016/j.jcp.2012.07.003>.
- Toimil, A., Losada, I.J., Nicholls, R.J., Dalrymple, R.A., Stive, M.J.F., 2020. Addressing the challenges of climate change risks and adaptation in coastal areas: A review. *Coastal Engineering* 156, 103611. <https://doi.org/10.1016/j.coastaleng.2019.103611>.
- Tuković, Ž., Karač, A., Cardiff, P., Jasak, H., Ivanković, A., 2018. Openfoam finite volume solver for fluid-solid interaction. *Transactions of FAMENA* 42, 1–31. <https://doi.org/10.21278/TOF.42301>.
- Weller, H.G., Tabor, G., Jasak, H., Fureby, C., 1998. A tensorial approach to computational continuum mechanics using object-oriented techniques. *Computers in Physics* 12. <https://doi.org/10.1063/1.168744>.
- Young, W.C., Budynas, R.G., Sadegh, A.M., 2012. *Roark's formulas for stress and strain*. McGraw-Hill Education.

## Fully-coupled hydroelastic modelling of a deformable wall in waves

Zhengyu Hu, Luofeng Huang, Yuzhu Li

### Highlights

- The hydroelastic interaction between periodic waves and an elastic vertical wall is investigated using an advanced computational approach.
- The structural stiffness and the ratio of the wave frequency to the wall's natural frequency can largely affect the wave-wall interaction.
- Empirical formulae are proposed for wave run-up, loading, and wall displacement in periodic waves.
- Optimization of flexibility is performed considering the wave transmission and the stress within the vertical elastic wall.
- The effect of the material damping is found to be negligible on periodic waves interacting with an elastic wall.

## Author Credit Statement

“Fully-coupled hydroelastic modelling of a deformable wall in waves”

Authors: Zhengyu Hu, Luofeng Huang, Yuzhu Li

**Zhengyu Hu:** Investigation, Data Curation, Writing-Original draft preparation, Code development

**Luofeng Huang:** Code development assistance, Writing- Reviewing and Editing, Methodology

**Yuzhu Li:** Conceptualization, Methodology, Writing- Reviewing and Editing, Supervision, Supercomputer resources acquisition, Funding acquisition

**Declaration of interests**

The authors declare that they have no known competing financial interests or personal relationships that could have appeared to influence the work reported in this paper.

The authors declare the following financial interests/personal relationships which may be considered as potential competing interests:

Journal Pre